JACS Au
AN OPEN ACCESS JOURNAL OF THE AMERICAN CHEMICAL SOCIETY

pubs.acs.org/jacsau
Article

Fusion Dynamics and Size-Dependence of Droplet Microstructure in ssDNA-Mediated Protein Phase Separation

Yunqiang Bian,[‖] Fangyi Lv,[‖] Hai Pan,[‖] Weitong Ren, Weiwei Zhang, Yanwei Wang, Yi Cao, Wenfei Li,* and Wei Wang*

Cite This: *JACS Au* 2024, 4, 3690−3704

Read Online

ACCESS | Metrics & More | Article Recommendations | Supporting Information

ABSTRACT: Biomolecular condensation involving proteins and nucleic acids has been recognized to play crucial roles in genome organization and transcriptional regulation. However, the biophysical mechanisms underlying the droplet fusion dynamics and microstructure evolution during the early stage of liquid−liquid phase separation (LLPS) remain elusive. In this work, we study the phase separation of linker histone H1, which is among the most abundant chromatin proteins, in the presence of single-stranded DNA (ssDNA) capable of forming a G-quadruplex by using molecular simulations and experimental characterization. We found that droplet fusion is a rather stochastic and kinetically controlled process. Productive fusion events are triggered by the formation of ssDNA-mediated electrostatic bridges within the droplet contacting zone. The droplet microstructure is size-dependent and evolves driven by maximizing the number of electrostatic contacts. We also showed that the folding of ssDNA to the G-quadruplex promotes LLPS by increasing the multivalency and strength of protein−DNA interactions. These findings provide deep mechanistic insights into the growth dynamics of biomolecular droplets and highlight the key role of kinetic control during the early stage of ssDNA−protein condensation.

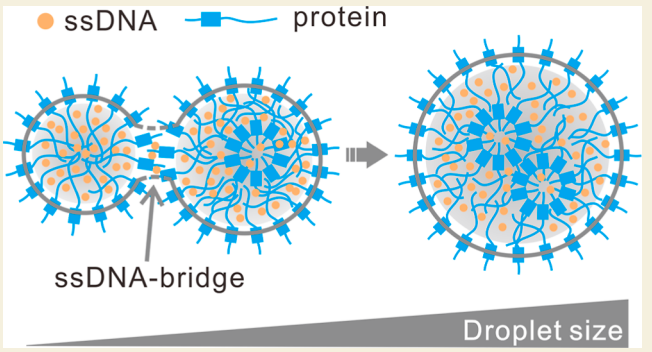

KEYWORDS: *biomolecular condensation, liquid−liquid phase separation, fusion, molecular dynamics, G-quadruplex, linker histone H1*

INTRODUCTION

Biological condensates formed by liquid−liquid phase separation (LLPS), in which biomolecules in solutions spontaneously separate into coexisting dilute and dense phases, are considered to play essential roles in myriad cellular processes, such as the stress responses, ribosome biogenesis, DNA damage repair, and chromatin organization.[1−14] These membrane-less condensates not only provide a favorable environment for biomolecules to establish interaction networks efficiently but also contribute to homeostasis through the concentration buffering effect. Aberrant condensation, on the other hand, can be involved in the pathogenesis of numerous neurodegenerative diseases. Therefore, unraveling the key physiochemical factors that regulate the structure and dynamics of biological condensates is crucial for understanding the biophysical basis underlying the biologically and pathologically relevant molecular events.[15−18]

It has been well established that multivalent weak interactions play a central role in driving LLPS.[4] Proteins containing intrinsically disordered regions (IDRs) of low-sequence complexity possess inherent multivalency and are widely engaged in the formation of membrane-less condensates. Such weak and multivalent interactions render the biological condensates dynamic and exchangeable with the surrounding cellular environment. Thus, the structure and dynamics of the condensates can be readily altered by various physiochemical factors or stimuli, such as pH, salt concentration, molecular crowding, protein folding/ligand binding, and post-translational modifications, which can potentially contribute to the regulation of cellular processes.[19−33] The phase behavior can be further enriched by sequence segregation of IDRs, resembling the block copolymer, and by heterotypic intermolecule interactions of multicomponent systems, which often leads to the microphase separation and layered structures of condensates.[34]

Nucleic acid molecules, which are highly charged, are key inducers or regulators of biological condensation mainly through intermolecule Coulombic interactions.[8,9,35−41] Because of the complex phase behavior and their biological prevalence, such multicomponent systems containing DNA and RNA received increasing attention. A well-documented

Received: August 3, 2024
Revised: August 27, 2024
Accepted: August 27, 2024
Published: September 4, 2024

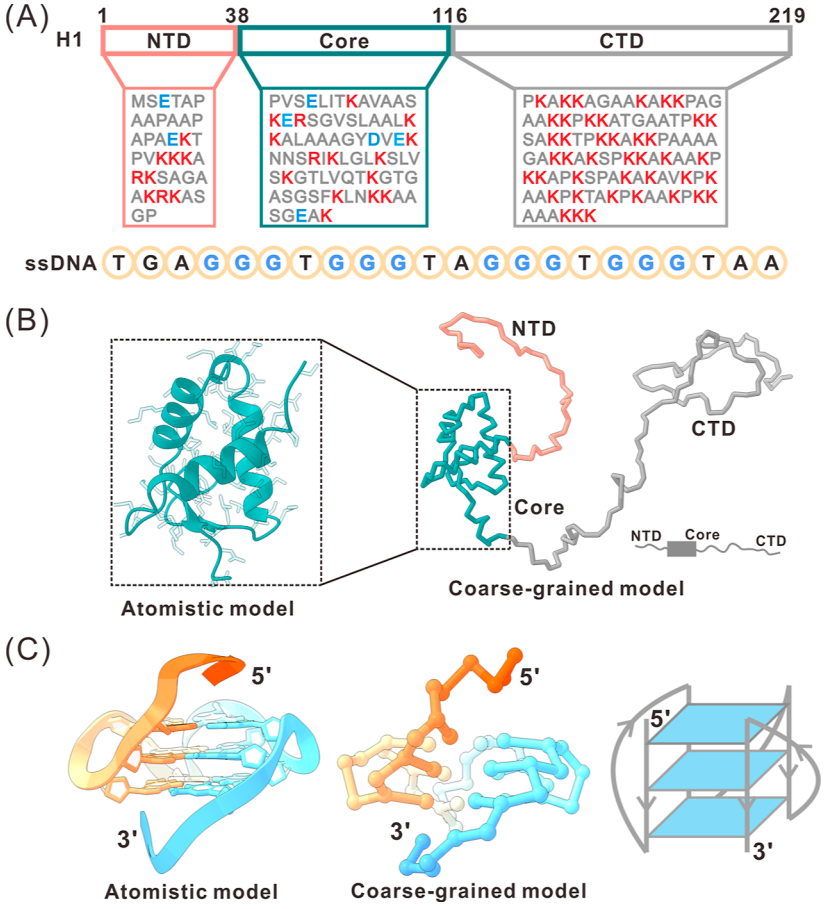

Figure 1. Simulation system. (A) Sequences of H1 and ssDNA (Pu22). Positively charged residues are colored red and negatively charged residues are colored blue. Guanine nucleotides forming the G4 structure are highlighted in blue. (B,C) Three-dimensional structures of H1 and G4 ssDNA used in the simulations. For each molecule, the atomistic model and the coarse-grained model are displayed, along with a schematic representation of the structure.

example is that the presence of RNA molecules can promote the LLPS of fused in sarcoma (FUS), which has been considered to be a critical nucleation step in the formation of pathological aggregates of neurodegenerative disorder diseases.[12,40,41] In addition, both experimental and computational studies showed that the co-condensation of protein and DNA/RNA tends to form a layered multiphasic microstructure. Recently, the significance of single-stranded DNA (ssDNA) as a crucial mediator in diverse phase separation processes of proteins has been increasingly appreciated.[20,36,42−47] ssDNA has been involved in nearly all genomic processes, such as transcription, replication, and DNA damage repair. Through specific or nonspecific recognition and binding interactions with proteins, they can promote phase separation and facilitate the assembly of protein condensates. In a recent experimental report, Leicher and co-workers found that ssDNA can mediate enhanced condensation of linker histone H1, which is among the most abundant chromatin binding proteins.[44] The ssDNA-induced H1 condensation can also be observed in vivo around replication forks, which is likely involved in DNA damage responses. Although these pioneer studies on the ssDNA-regulated protein phase separation have provided significant new insights into the molecular mechanism of DNA−protein co-condensation, several important questions regarding the growth dynamics and microstructure of the ssDNA−protein condensates remain unclear, including the following: (i) what physical interactions dictate the fusion of liquid droplets; (ii) how the droplet microstructure and stoichiometry evolve with fusion at the early stage of condensation; and (iii) how the ssDNA folding regulates the ssDNA−protein co-condensation.

In this study, we address the above questions by investigating the guanine-rich ssDNA induced condensation of linker histone H1 using residue-resolved molecular dynamics (MD) simulations. Guanine-rich DNA sequences have a tendency to adopt unique structural arrangements called G-quadruplexes (G4s), which have been found to play crucial roles in diverse biological processes, such as regulation of gene expression and maintenance of genome integrity.[48] It was considered as potential target of drug design for cancer therapy.[49] Since G4-forming sequences are highly prevalent in heterochromatin regions, the co-condensation between DNA quadruplex and the linker histone H1 can be involved in the chromatin condensation and gene expression regulation.[50] In addition, it also provides a model system for investigating the general mechanism underlying the molecular process of ssDNA induced phase separation. In a recent experimental report, Mimura et al. showed that ssDNA folding tends to promote the growth of the ssDNA-H1 condensate and slow down the molecular motility within the droplet.[47] The importance of G4 structure in inducing the droplet formation in cell was also demonstrated by using biomimetic protocells, which showed a temperature-dependent reversible microphase separation of guanine-rich ssDNA and its binding protein.[51] Despite its biological significance, computational studies of the

https://doi.org/10.1021/jacsau.4c00690
JACS Au 2024, 4, 3690−3704

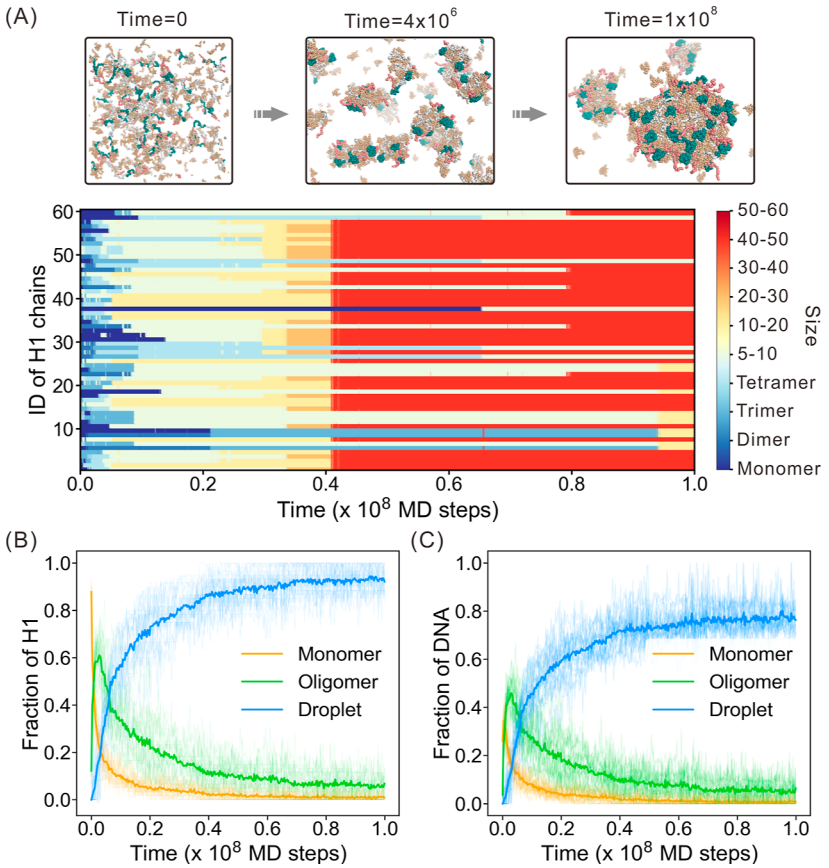

Figure 2. Molecular processes of the early stage of ssDNA-H1 co-condensation. (A) Representative simulation trajectory capturing the condensation of H1 under the regulation of ssDNA. Representative snapshots of the MD simulation trajectory at different time points are shown in the upper panel. The cluster size to which each H1 chain belongs during the simulation process is shown in the lower panel. The NTD, core domain, and CTD of H1 is colored as red, green, and white, respectively. The ssDNA is colored as wheat. (B) Fraction of H1 in free monomers, oligomers, and droplets as a function of simulation time. (C) Fraction of ssDNA in free monomers, oligomers, and droplets as a function of simulation time.

G4 coupled phase separation are still lacking to our best knowledge. By performing MD simulations, we can directly identify the key physical interactions contributing to the droplet fusion and the formation of microstructures in the condensates, which is otherwise challenging in experimental studies. We showed that the surface of the droplet formed by the ssDNA and H1 is occupied by the modestly charged N-terminal domain (NTD) and globular domain (core domain), whereas the highly charged C-terminal domain (CTD) is deeply buried inside the droplet together with ssDNA. The fusion of droplets is triggered by the formation of ssDNA-bridge, in which one ssDNA molecule simultaneously forms electrostatic contacts with the positively charged H1 core domains from the surfaces of two fusing droplets, demonstrating the crucial role of kinetic control in droplet fusion. We also revealed a size dependence of the microstructure of the droplets, which is dictated by the maximization of the charge−charge interactions between the CTD and ssDNA. In addition, we showed that the folding of the ssDNA to the G4 structure increases the local charge density and contributes to the enhanced LLPS. These results provide new insights into the general biophysical mechanism underlying the ssDNA coupled biological phase separation.

RESULTS

Growth of Condensate by Coalescence of Smaller Clusters

Linker histone H1 is a typical IDR protein. It consists of a short unstructured NTD, a conserved core domain and a long disordered CTD (Figure 1A,B).[45] The CTD is rich in lysine residues and, therefore, highly positively charged. The NTD and core domain are also positively charged but are much more moderate. For the ssDNA, we used the 22 nt oncogene c-myc promoter ssDNA sequence Pu22 (d-[TGAGGGTGGGTAGGGTGGGTAAA]),[52] which is known to fold to a parallel G4 topology (Figure 1A,C) and was observed to promote the phase separation of H1.[47] Unless otherwise stated, ssDNA represents single-stranded DNA with the G4 conformation hereafter.

To obtain a comprehensive understanding of the phase separation dynamics, we performed 20 independent simulations in the canonical ensemble with constant chain number, volume, and temperature (*NVT*) for a system comprising 60 H1 chains and 300 ssDNA chains. This stoichiometry was chosen since it can induce phase separation prominently as shown in previous experiment.[47] Molecular simulations also showed that insufficient or excessive addition of ssDNA tend to inhibit cluster growth (Figure S1). The initial state of the system was prepared by randomly placing the biomolecules in a periodic cubic box with the size of 650 Å × 650 Å × 650 Å.

https://doi.org/10.1021/jacsau.4c00690
JACS Au 2024, 4, 3690−3704

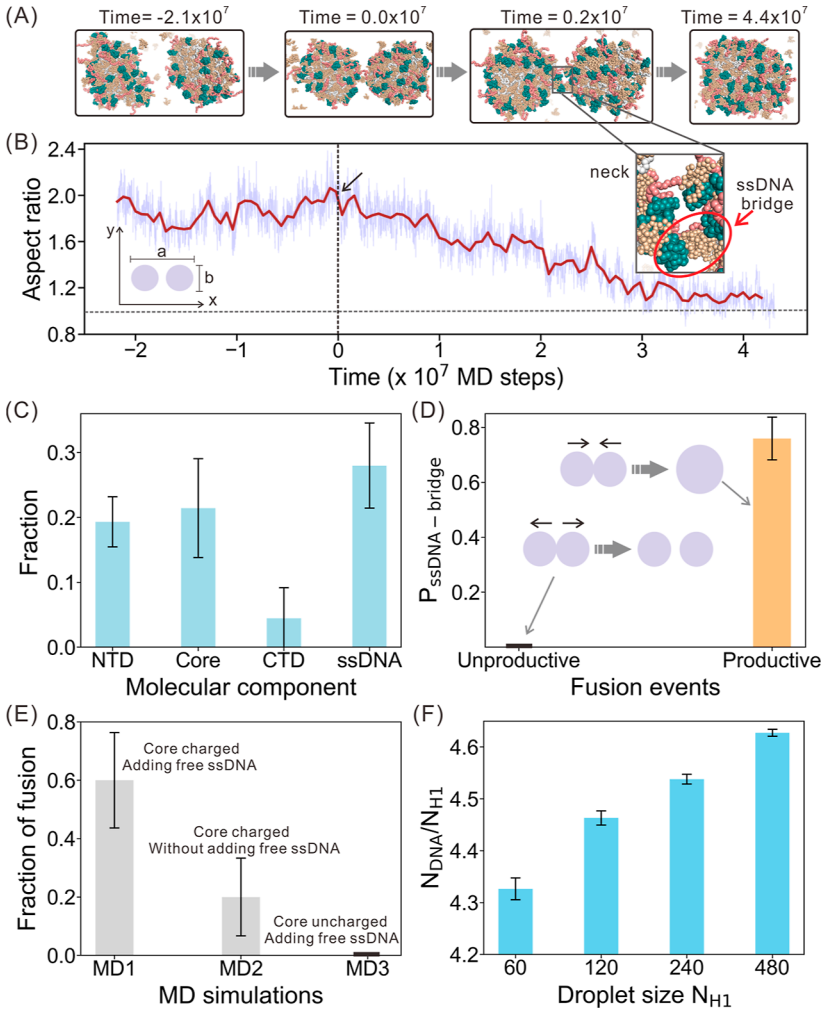

Figure 3. Molecular simulations of droplet fusion. (A) Snapshots along a representative trajectory of successful fusion event. The ssDNA-bridge in a neck-like region is highlighted. (B) Aspect ratio of the fusing droplets as a function of simulation time for the fusion event shown in panel (A). The time step at which the two droplets initially came into contact was set as zero. The aspect ratio is given by the ratio of the longest axis (a) to the shortest axis (b) in the *xy*-plane. (C) Fraction of different components in the neck-like region formed by the fusing droplets. (D) Probabilities of ssDNA-bridge formation in the unproductive and productive fusion events. The probability in the unproductive fusion events is zero and labeled by a black bar. (E) Fraction of trajectories successfully captured the fusion events in three sets of simulations. The fraction in MD3 is zero. (F) Molar ratio of the ssDNA and protein in the droplets with different sizes. The droplet size is characterized by the number of H1 chains (N_{H1}) contained in the droplet.

Figure 2A shows a representative trajectory that effectively captured the transition of H1 chains from free monomers to larger condensates together with ssDNA molecules over time, which can provide an insightful understanding of the formation and growth dynamics of the droplet. Initially, the protein molecules exhibit a transition from individual monomers to various small clusters, indicating their tendency to immediately condense upon initialization. As the simulation progresses, these small clusters further assemble and coalesce as implied by the sharp increases in cluster size, leading to the formation of larger condensates. Once formed, these larger condensates hardly dissolve, suggesting that Brownian coalescence,[53] not Ostwald ripening,[54] dominates the fusion events in the simulations. We also conducted similar simulations for the system only containing H1 chains, and no large condensates were observed.

In further analysis for the overall 20 simulation trajectories, we categorized the assembled clusters into three distinct groups based on the number of constituent H1 chains (N_{H1}), including monomers ($N_{H1} = 1$), oligomers ($1 < N_{H1} \leq 4$), and condensates ($N_{H1} > 4$). Throughout this work, we used N_{H1} to describe the droplet size. By adopting this classification, we were able to obtain a more comprehensive characterization of the condensation dynamics. Figure 2B illustrates the fraction of H1 chains presented in the three classes of assembly clusters throughout the simulations. The fraction of H1 chains in the monomeric state decreases monotonically over time. This is a direct consequence of the phase separation, as the H1 chains undergo condensation to form larger assemblies. Conversely, the fraction of H1 chains in droplet state increases monotonically. In contrast to the monotonic evolution of the monomeric state and droplet state, the fraction of H1 chains in oligomers exhibits a different pattern during the simulations. It reaches a peak value rapidly at the beginning of the simulations and then decreases as time progresses. Remarkably, the decrease in the fraction of H1 chains in oligomers coincides with the increase in the fraction of H1 chains in droplets. This observation supports the notion that the formation of larger droplets arises

https://doi.org/10.1021/jacsau.4c00690
JACS Au 2024, 4, 3690−3704

from the collision and fusion of smaller ones as suggested by the Brownian coalescence mechanism of droplet growth.[53,55] The merging of smaller droplets contributes to the growth of more stable structures. The time evolution of the fraction of ssDNA molecules in the three types of assemblies exhibited a similar pattern (Figure 2C), which is a result of the ssDNA-H1 co-condensation.

Kinetic Control in Droplet Fusion Dynamics

The above simulations clearly demonstrated the importance of the fusion of small clusters in droplet growth. To gain a deeper understanding of the fusion dynamics involved in droplet growth, we conducted an additional set of 10 independent simulations specifically focusing on the fusion process of two droplets (MD1). In constructing the system for fusion simulations, we selected a droplet (N_{H1} = 40) formed in the above simulations and then placed two copies with significant spatial separation in a cubic box (700 Å × 700 Å × 700 Å). In the droplet selected above, the molar ratio between ssDNA and H1 is lower than the average molar ratio (5.0) of the initial simulation system. To maintain the overall molar ratio intact, additional free ssDNA molecules were randomly added to the fusion simulations. Figure 3A shows the instantaneous conformations at various time points in a representative trajectory that successfully captured the fusion event. For this trajectory, we also monitored the shape change of the system formed by the component droplets over time by estimating the aspect ratio (Figure 3B). A significant decrease in aspect ratio was observed in the fusion simulations, indicating a transformation from separated droplets to a more spherical fused droplet. This observation demonstrates that the MD simulations can capture the main feature of the fusion events. Overall, out of the 10 trajectories examined, six successfully captured the full fusion event between two droplets within a simulation length of 5×10^7 MD steps (Figure S2).

As depicted in Figure 3A, once the two droplets initially made contacts, a neck-like contacting zone emerged. The presence of this neck-like structure is crucial for understanding the molecular mechanism of droplet fusion. To examine the composition and interaction features of this region, the fractions of different molecular components were analyzed, which showed that the neck region was rich in NTD, core domain, and ssDNA (Figure 3C), whereas the CTD is rare. Interestingly, the simulation trajectory showed that the fusion events are intrinsically stochastic because two droplets were demonstrated to not always coalesce successfully (Figure S3). Even though two droplets come close and form a contacting zone, it may either evolve to a fused droplet as shown in Figure 3A (productive) or spontaneously separate again (unproductive). Remarkably, the productive fusion event relies on the formation of an ssDNA-bridge wherein one ssDNA simultaneously forms contacts with two NTD/core domains from different fusing droplets (Figure 3A). For the productive fusion events, the probability of observing the ssDNA-bridge in the contacting zone of the sampled snapshots is larger than 0.7, whereas the probability is zero for the unproductive fusion events (Figure 3D). Based on these observations, it can be inferred that the ssDNA bridged interactions between the fusing droplets play a crucial role in facilitating subsequent coalescence, suggesting the crucial role of kinetic control in the droplet fusion events.

As a further demonstration of the key role of the ssDNA-bridge in droplet fusion, we conducted two additional sets of control simulations (Figure 3E). In the first set of simulations (MD2), there is no free ssDNA molecules being added to the simulation box. In comparison to the simulation results shown above (MD1), we observed a noticeable decrease in fusion ability. Out of the 10 simulations conducted, only two successfully captured fusion events (Figures 3E and S2). This decrease in the fusion ability suggests again that the presence of free ssDNA molecules, which can accumulate onto the droplet surface, may play an important role in promoting efficient droplet fusion. The removal of these molecules appears to hinder the formation of the ssDNA-bridge as discussed above. In addition, the presence of free ssDNA may also neutralize the surface charges of the droplets and therefore weaken the electrostatic repulsion during the approaching phase of the fusion event. In the second set of simulations (MD3), the charges of the residues in the core domain are neutralized. This structured core domain, which is the most prevalent component on droplet surface, contains multiple positively charged residues, and it is the main participant of the ssDNA-bridge. We observed that none of the trajectories captured droplet fusion event among the 10 simulations (Figures 3E and S2), which highlights again the crucial role of ssDNA-bridge formed in the contacting zone in promoting efficient droplet fusion and growth. To further support the above MD simulation results, we also performed multiple sets of experiments to investigate the effect of adding free ssDNA on droplet growth. The results demonstrate that introducing additional ssDNA into the solution of ssDNA and H1 after an incubation period leads to the emergence of larger droplets (Figure S4), demonstrating the kinetic role of the added extra ssDNA in promoting the droplet growth.

The above MD simulation results clearly demonstrate that ssDNA-bridge coupled kinetic control plays a crucial role in the droplet fusion and growth process. Furthermore, we observed that the preferred stoichiometry of the droplets depends on their sizes. For example, the molar ratio between ssDNA and H1 is ∼4.3 in the small droplet used in the above fusion simulations, which is much lower than the initial ratio (5.0). After the fusion of the two small droplets in the MD1 simulations, the molar ratio of the droplet becomes larger than 4.4 (Figure S5), which may suggest that larger droplet prefers a stoichiometry with higher ssDNA content. As a further characterization of the size dependence of the droplet stoichiometry, we performed additional droplet simulations, which generated the droplets with various sizes (see the Materials and Methods section for more details). In line with the above observations, the results showed that as the droplets grew in size, the molar ratio between ssDNA and H1 in the droplets tends to increase (Figure 3F). Such droplet size dependence of the stoichiometry suggests that the preferred molar ratio of the ssDNA and protein for droplet fusion changes with time, demonstrating again the key role of kinetic control in droplet growth.

Microstructure of Condensates Is Size-Dependent

The interactions between the biomolecules within the condensate dictate its microstructure and biological function.[56] Therefore, we also performed a detailed characterization of the droplet microstructure formed by H1 and ssDNA. For the droplet (N_{H1} = 40) used in the fusion simulations, we calculated the radial distribution function of the mass density. The results revealed a core−shell-like structure of the droplet (Figure S6). Specifically, the NTDs and core domains of H1

https://doi.org/10.1021/jacsau.4c00690
JACS Au 2024, 4, 3690−3704

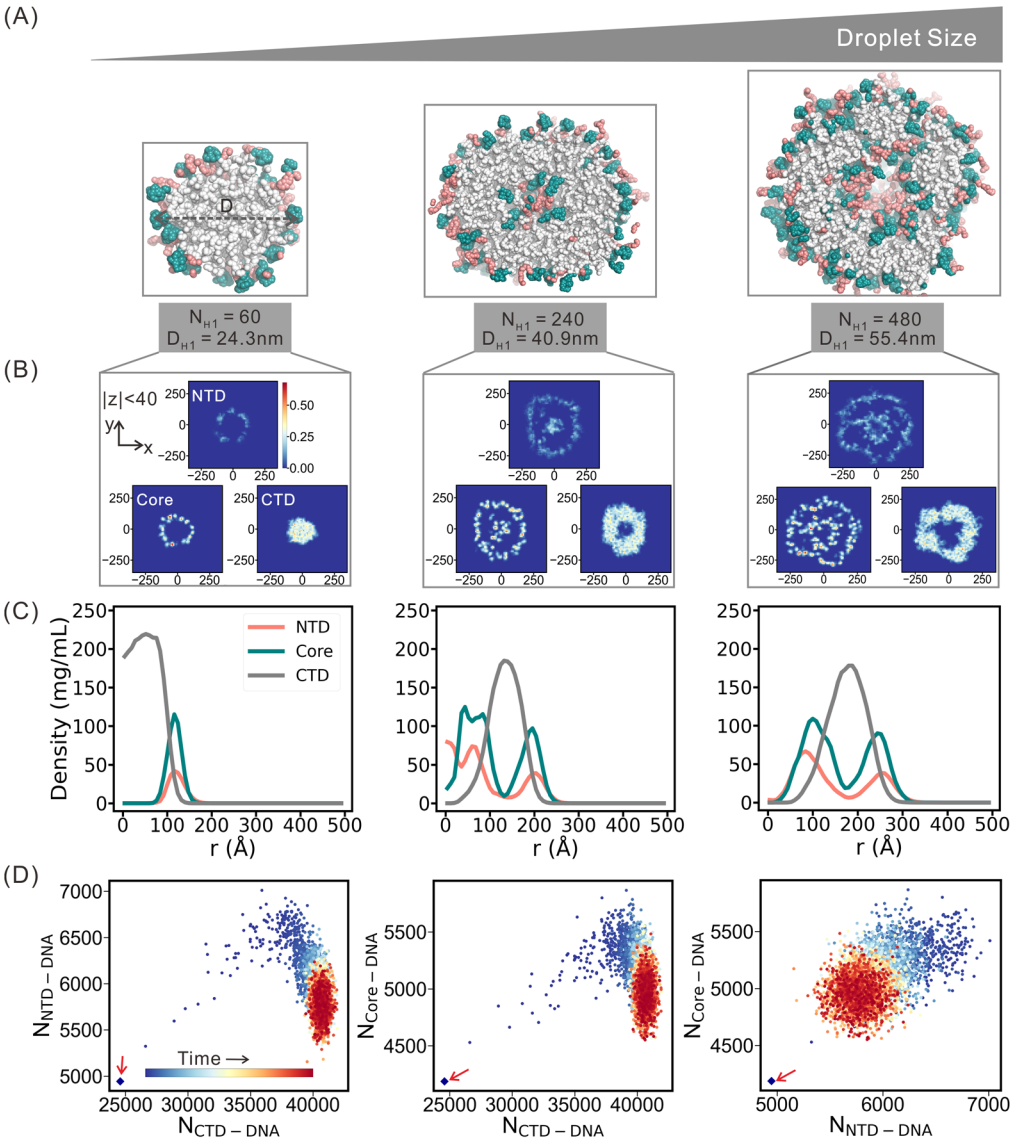

Figure 4. Size-dependence of the droplet microstructure. (A) Structural profiles for three representative conformations of droplets with different sizes (N_{H1} = 60, 240, and 480, which have the diameters of 24.3, 40.9, and 55.4 nm, respectively). Only the H1 molecules are displayed to ensure a clear visualization. (B) Distribution probabilities of the three domains of H1 within a slice of the droplets ($|z| \leq 40$). (C) Radial distribution of the mass density for the three domains of H1. (D) Trajectory of droplet simulations with the droplet size of N_{H1} = 480 projected along the reaction coordinates ($N_{CTD-DNA}$, $N_{NTD-DNA}$), ($N_{CTD-DNA}$, $N_{NTD-DNA}$), and ($N_{CTD-DNA}$, $N_{NTD-DNA}$). Here, $N_{CTD-DNA}$, $N_{NTD-DNA}$, and $N_{core-DNA}$ describe the number of formed contacts between ssDNA and the three domains of H1 within the droplet. The starting point is indicated by red arrow.

form a shell-like arrangement encasing a core composed of CTDs and ssDNA molecules, as also illustrated by the structural profile of the droplet.

To further investigate whether such a core−shell-like structure is maintained for larger droplets, we also conducted structural analysis on the droplets of different sizes generated by the above droplet simulations. In the case of the droplet with N_{H1} = 60, a core−shell structure similar to the one observed above within a smaller droplet (N_{H1} = 40) was identified as shown by the droplet structural profile and spatial distribution of different H1 domains (Figure 4A−C, left). However, as the droplet further increases in size, distinct structural changes become evident. The primary structural transformation observed during droplet growth involves an increased condensation of NTD and core domains toward the interior of the droplet (Figure 4A−C, middle). Additionally, as the droplets continue to enlarge, further microphase separation occurs, leading to additional structural variations. For example, in the case of a large droplet with N_{H1} = 480, the NTDs and core domains adopt a hollow-like microphase structure (Figure 4A−C, right), which is in contrast to the clustered substructure observed in a droplet with N_{H1} = 240. Furthermore, in a significantly larger droplet (N_{H1} = 960), these molecular components can undergo distinct microphase separation, resulting in the formation of various NTD/core clusters within the interior of the droplet (Figure S7). These findings suggest that the condensed structure within the droplets may exhibit a size-dependent nature. In other words, as the droplet size increases, the structural organization and composition of the component biomolecules can undergo large changes, which may have significant implications for the regulation of biological processes.

To confirm that the clusters are droplets rather than aggregates, we calculated the mean square displacement of H1

https://doi.org/10.1021/jacsau.4c00690
JACS Au 2024, 4, 3690−3704

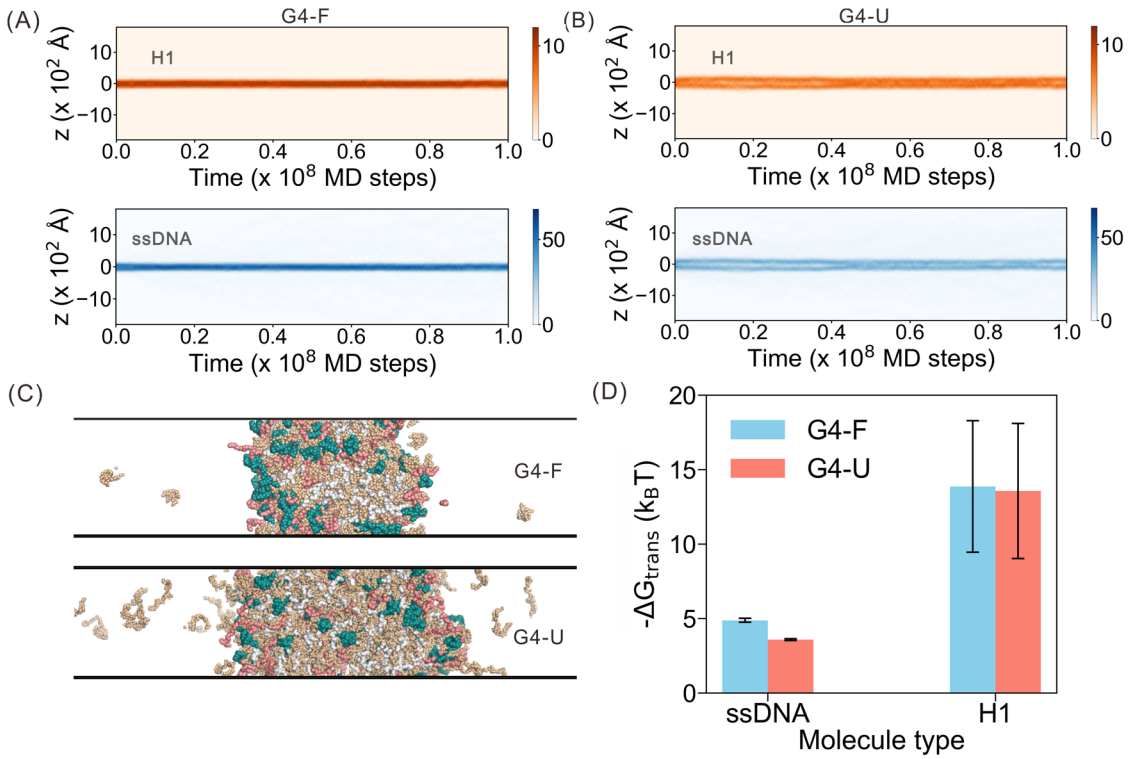

Figure 5. Effect of ssDNA folding on phase separation. (A,B) Density profiles of H1 and ssDNA in the slab simulation trajectory for the systems G4-F (left) and G4-U (right) at 300 K. (C) Representative snapshots of the slab simulations for the systems G4-F (upper) and G4-U (lower), respectively. (D) Saturation concentrations of the ssDNA and H1 estimated from the slab simulations for the systems G4-F (blue) and G4-U (red), which correspond to the concentrations in the dilute phase.

and ssDNA chains in the droplet with N_{H1} = 480 to estimate the mobilities of these molecules. As shown in Figure S8, both H1 and ssDNA could diffuse significantly along wide range of the cluster, although H1 diffuses relatively slower due to its larger size. This result implies that the molecules within the condensate formed by H1 and ssDNA are dynamic and liquid-like. In addition, the confocal fluorescence microscope monitoring the droplet fusion event also illustrated the high mobilities of the ssDNA chains among the droplet (Figure S9).

The above size dependence of the droplet microstructure can be understood based on the maximization of the electrostatic contacts between the highly charged CTDs and ssDNA. According to the sequence feature of H1, the CTD is highly charged, and therefore the contact formation of CTD with the oppositely charged ssDNA is energetically favored. For the droplet with a small size, such an energetic requirement can be easily satisfied when the CTD and ssDNA are buried in the interior of the droplet, whereas the NTD and core domain are exposed to the droplet surface. However, with the growth of the droplet size, CTD and ssDNA cannot occupy the full interior of the droplet. In this case, the NTD and core tend to form clusters in the interior of the droplet to maximize the favorable CTD-ssDNA contacts and therefore minimize the energetic frustration.[34,57,58] The increasing of the contact number between the CTD and ssDNA during the simulations of the droplets with different sizes (Figures 4D and S10) clearly demonstrate the above energetic rule for the formation of droplet microstructure.

Quadruplex Folding Promotes LLPS by Increasing the Multivalency and Strength of Protein–DNA Interactions

The three-dimensional structures of protein and nucleic acid have the potential to affect the behavior of phase separation.[56] Next, we focused on investigating the effect of the ssDNA conformation on LLPS by comparing the phase separation behaviors induced by folded and unfolded G4 structures. For simplicity, the simulation systems with the ssDNA being folded and unfolded are termed G4-F and G4-U, respectively. First, we conducted slab simulations at 300 K for the ssDNA-H1 mixture with the same molar ratio as the above simulations. For both the G4-F and G4-U systems, two distinct phases were observed, i.e., dilute phase and condensed phase (Figure 5A,B), suggesting their capability of undergoing phase separations. However, compared to the G4-U system, the G4-F system demonstrated lower saturation concentrations (C_{sat}) at the dilute phase but a higher concentration at the condensed phase (Figure 5C,D). Such results imply that the system with the ssDNA folded into G4 structure is more prone to undergo phase separation, which is consistent with experimental observations.[47] In addition, the slab simulations show that the molar ratio between ssDNA and H1 in the condensed phase (~4.8, Figure S11) is lower than those in the dilute phase (>5.0), consistent with the results of the above droplet simulations. Since the slab simulation system corresponds to an infinite system due to periodic conditions, these results suggest that the N_{DNA}/N_{H1} ratio shown in Figure 3F may approach 4.8 as the droplets continually grow in size. Compared to the G4-F system, the molar ratio of the condensed phase for the G4-U system is lower (Figure S11).

https://doi.org/10.1021/jacsau.4c00690
JACS Au 2024, 4, 3690−3704

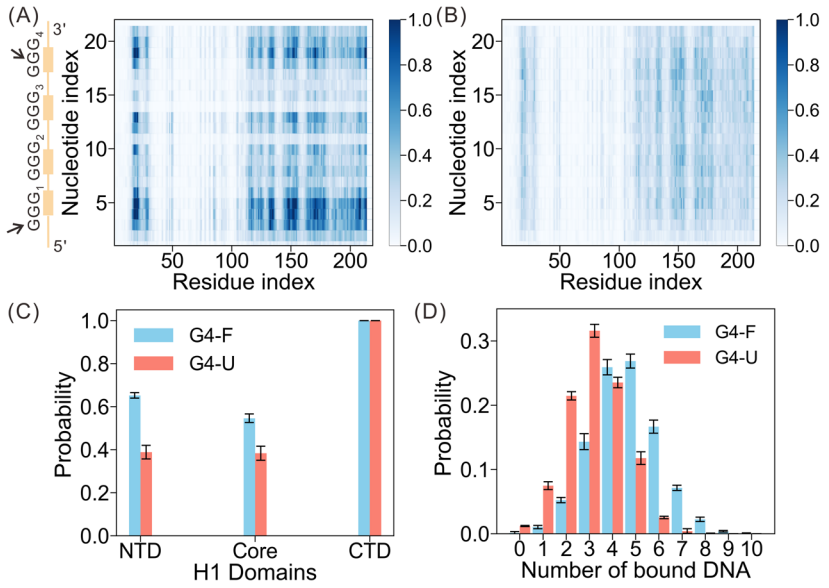

Figure 6. Effect of ssDNA folding on the ssDNA-H1 interactions. (A,B) Probabilities of the contact formation between the residues H1 residues and ssDNA nucleotides for the systems G4-F (A) and G4-U (B). (C) Probabilities of ssDNA binding with the NTD, CTD, and Core domain of H1 for the systems G4-F (blue) and G4-U (red). (D) Distribution probability of the number of ssDNA molecules bound to one H1 chain for the systems G4-F (blue) and G4-U (red).

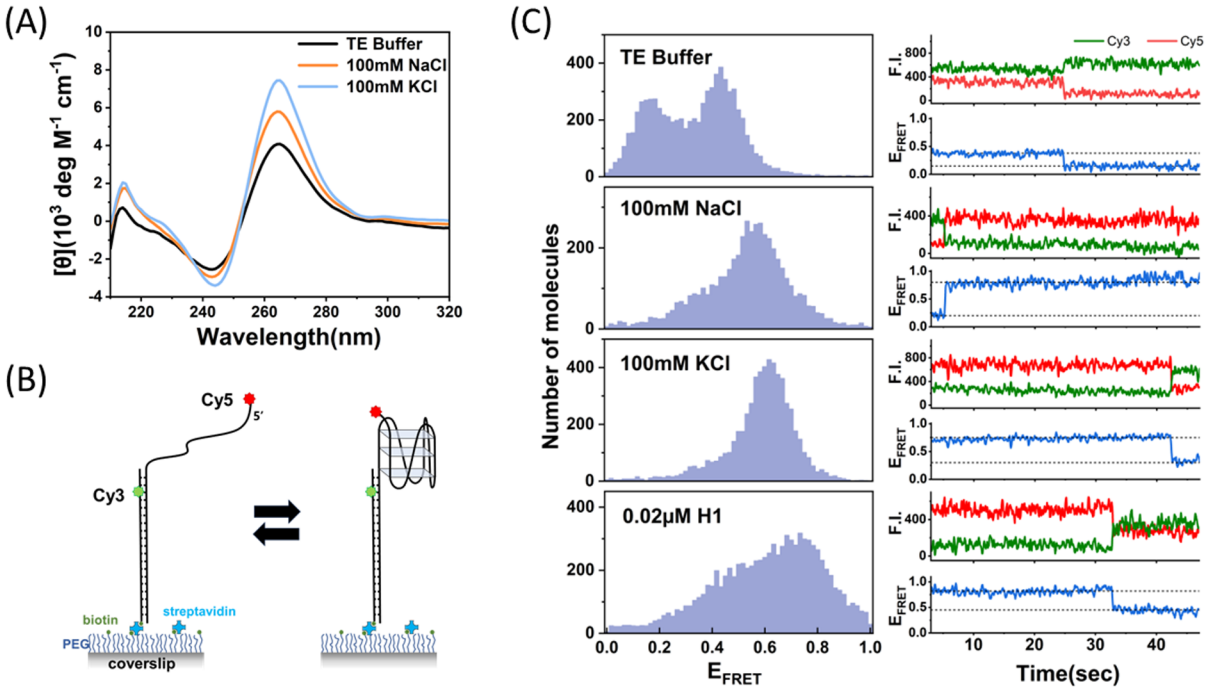

Figure 7. Experimental characterization of the effect of salt and H1 on the conformational feature of ssDNA. (A) CD spectra of ssDNA under different conditions. (B) Schematic illustration for the smFRET setup. (C) Histograms of smFRET efficiency in the presence of TE buffer only, with the addition of 100 mM NaCl or 100 mM KCl, and with the presence of H1 (left). The representative smFRET trajectories were also shown accordingly (right).

To further understand the key role of G4 folding on the LLPS, we performed additional simulations for the G4-F and G4-U systems containing one H1 chain and 40 ssDNA chains and analyzed the interaction pattern at the residue-level. We first calculated the contact probabilities between the residues of H1 and the nucleotides of ssDNA (Figure 6A). The contact map revealed that H1 in the G4-F system tends to interact with the G4 groove between two GGG-repeats, i.e., GGG_1 and GGG_4, which are positioned at the 5′-terminal and 3′-terminal, respectively (Figures 6A and S12). In contrast, no distinct binding pattern was observed for the G4-U system (Figure 6B). In addition, it was observed that folded G4 exhibits a greater affinity for binding to both the NTD and core domain of H1, as illustrated by the increased contact probability (Figure 6C). These findings collectively indicate that the folding of G4 structure enhances the ability of ssDNA to bind to proteins. Furthermore, it was observed that a single chain of H1 can attach to more ssDNA molecules in the G4-F system

https://doi.org/10.1021/jacsau.4c00690
JACS Au 2024, 4, 3690−3704

compared to that in the G4-U system (Figure 6D). More detailed analysis showed that all the three H1 domains can contribute to the enhanced binding of the folded G4, with the CTD has more pronounced effect (Figure S13A,E). The interactions between H1 and ssDNA in the droplets demonstrate the similar interaction feature (Figure S13F,G). The contact maps between H1 and ssDNA showed that the H1 tends to make contacts with the GGG-strands of the folded G4 (Figures 6A,B and S14). Overall, these observations suggest an increase in the interaction multivalency and strength between the protein and ssDNA upon G4 folding. One possible reason for the enhanced interaction is that the folding of G4 tends to better align the charged phosphate groups and provide a scaffold for efficient binding of H1, leading to the increased interaction multivalency between H1 and ssDNA.

The above slab simulations focus on two extreme cases: the ssDNA chains are either fully folded (G4-F) or fully unfolded (G4-U). However, the ssDNA conformation can be dynamically modulated by binding to metal ions or H1 chains, which can, in turn, affect the phase separation behavior. Therefore, it is interesting to investigate in depth the effect of salt and H1 on the conformational feature of ssDNA experimentally. We first performed circular dichroism (CD) measurements of ssDNA with and without adding salt. We observed that adding KCl and NaCl can significantly increase the folding extent of the ssDNA (Figure 7A). For example, after adding KCl or NaCl with the concentration of 100 mM, the ellipticity at the wavelength of 264 nm increases dramatically, suggesting increased stability of the folded state, which is consistent with previous experimental results.[59] We then performed single-molecule fluorescence resonance energy transfer (smFRET) measurements of the ssDNA to further investigate the effect of salt and H1 binding on ssDNA folding (Figure 7B,C). The smFRET efficiency monitors the distance between the two ends of ssDNA, which therefore provides information on the ssDNA folding. One can see that the two ends of ssDNA become closer with the addition of NaCl or KCl as indicated by the higher smFRET efficiency, suggesting that adding salt tends to promote the folding of ssDNA, which is consistent with the CD results. Interestingly, we observed that the effect of H1 binding on the smFRET efficiency is very similar to that of adding salt, which suggests that H1 binding can also significantly increase the population of the folded conformation of ssDNA. Such observation is important and it implies that the phase separation can be coupled with the H1 binding induced ssDNA folding. In addition, as the ssDNA tends to adopt a folded conformation when bound with H1, the phase separation behavior may be more relevant to the above MD simulations with folded ssDNA. Interestingly, even though the isolated ssDNA chain tends to be partially unfolded without adding KCl or NaCl (Figure S15), the phase separation can be clearly observed and are even more prominent compared to the case with adding KCl or NaCl, possibly due to the H1 induced folding of ssDNA.

DISCUSSION AND CONCLUSIONS

Understanding the mechanism of fusion dynamics is crucial in gaining insights into the growth of biological condensates and related biological functions. It has been well established that the dynamics of droplet fusion are closely associated with the physical and material properties of the condensates, such as viscosity and surface tension, which in turn rely on the intermolecular interaction strengths and the structural compactness of component macromolecules.[60] In addition, recent studies revealed that the growth of biological condensates can also be regulated by modifying the droplet surface as a result of recruitment of additional biomolecules.[5,61,62] For example, experimental investigation of P granule growth showed that the recruitment of MEG-3 protein clusters to the granule surface can impede its growth.[5] In this work, we further revealed the critical role of the kinetic control in droplet fusion by investigating the early stage of the ssDNA-H1 co-condensation. The MD simulations directly demonstrated the stochastic collision and fusion processes of the droplets. The fusion event is productive only when an ssDNA chain simultaneously forms electrostatic contacts with the positively charged H1 core domains from the surfaces of two fusing droplets in the neck-like contacting zone. Such an ssDNA-bridge stabilizes the encounter complex of the two approaching droplets, which allows the establishment of more favorable interactions between the droplets for fusion. Adding extra ssDNA molecules largely promotes the fusion events since these free ssDNA chains tend to attach to the droplet surface and therefore have a higher probability to mediate the formation of the ssDNA-bridge compared to the ssDNA located at the interior of the droplets. Additionally, modifications on the residues of the H1 core domain by neutralizing the charge state were observed to result in a significant attenuation of the fusion ability because it directly breaks the ssDNA-mediated electrostatic interactions, demonstrating the crucial role of the ssDNA-bridge in regulating droplet fusion.

By adopting different shapes and arrangements, condensates can achieve specialized compartmentalization and provide distinct microenvironments in which biochemical reactions take place. It has been shown that these condensed structures are not always homogeneous.[2] For instance, condensates composed of multiple components have been observed to adopt core−shell structures, as observed in P granules and stress granules.[63,64] A recent experimental report revealed that FUS protein can also form condensates with a core−shell structural feature.[65] Additionally, certain condensates display hollow morphologies, such as the nuclear germ granules in Drosophila and nucleoprotein-RNA mixtures.[66,67] Furthermore, under certain conditions, these condensate structures can undergo further microphase separation. An example is observed in the presence of type II topoisomerase enzymes, where wall-like substructures can emerge through microphase separation within euchromatic domains, which form via the phase separation of chromatin.[68] Consistent with these observations, we identified an inhomogeneous structural feature within the condensate formed by H1 and ssDNA. Moreover, we discovered that the microstructure of the condensate is dependent on its size. This indicates that the physical properties and organization of the condensate may vary based on its overall dimensions. In smaller condensates, the constituent molecules tend to form core−shell-like structures. However, as the condensate grows in size, the microstructure of the droplet core can undergo further phase separation. This microphase separation within the core region of the condensate highlights the dynamic nature of biological condensates and suggests a complex interplay between molecular interactions and the overall organization of the condensate.

The microstructures formed within the biomolecular condensates have great biological significance.[69] For example,

https://doi.org/10.1021/jacsau.4c00690
JACS Au 2024, 4, 3690−3704

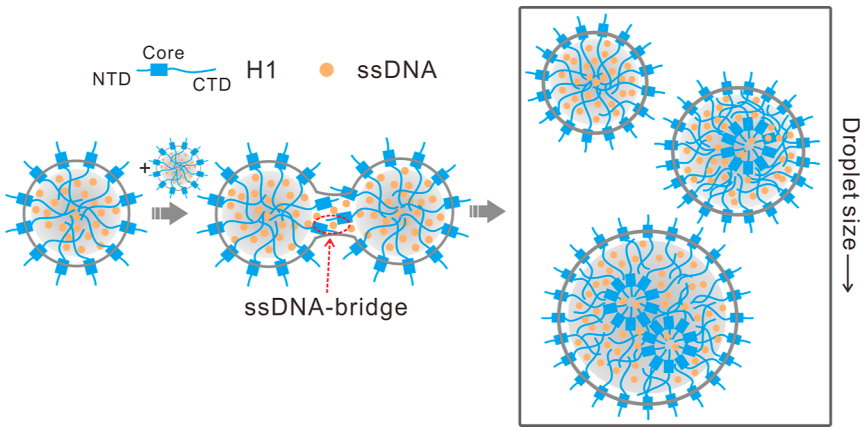

Figure 8. Schematic illustration showing the molecular mechanism of droplet fusion and growth. The ssDNA-bridge, which represents the bottleneck step for the productive fusion event, is highlighted by red circle.

the microstructure in P granule was found to be capable of providing a kinetic control of cellular processes (e.g., enzyme-catalyzed reactions).[63] For the ssDNA-H1 system studied in this work, the formation of microstructure has the potential to modulate the local environment and conformational feature of ssDNA. Such effects may contribute to the organization of heterochromatin and regulation of gene expression, considering the fact that the G4-forming sequence is prevalent in regions of heterochromatin, while H1 is a ubiquitous chromatin protein modulating nucleosome compaction.

Conformational changes of biomolecules can modify the intermolecular interactions, which may therefore alter the LLPS behavior and contribute to the regulation of biological processes. However, computational studies on the interplay between biomolecular conformational changes and LLPS are rather rare. An illustrative example in this context is the G4 folding, as studied in this work. The folding of G4 structures from ssDNA sequences was found to play a pivotal role in promoting phase separation. Our simulations successfully reproduced this experimental observation.[47] In addition, we observed that the folding of ssDNA into the G4 structures significantly influenced the strength of interactions between the G4 structures and the H1 protein within the condensate. Furthermore, this change in interaction strength was shown to have a profound impact on the multivalency of specific interactions between proteins and DNA. Since the saturation of interaction multivalencies controls the final size of the condensate,[70] the increased multivalency upon G4 folding allows the formation of larger condensates.

In this study, we mainly focused on the molecular event at the early stage of phase separation, and the investigated condensates have the length scale of <100 nm. Currently, investigating dynamics and structural features of the formed nanometer-scale condensates at the early stage of phase separation is still challenging in experiments. MD simulations provide a powerful tool to alleviate the resolution problem in characterizing the nanometer-scale condensates. By conducting extensive MD simulations, we provide insights into the underlying molecular mechanism that controls the droplet fusion events and the molecular-level structural information of the nanometer-sized condensates. It is worth noting that biomolecular condensates have been demonstrated to have various sizes. Especially, the biomolecular condensates with the sizes of tens to hundreds of nanometers are prevalent in cells and have been observed to play essential roles in regulating many key biological processes.[71−73] Therefore, the molecular mechanism elucidated in this work for the nanometer-sized condensates would be of biological relevance. As a supplementary to the molecular simulations, we also tried to characterize the nanoscale microstructure of the condensates by using a transmission electron microscope (Figure S16). We can observe the heterogeneity in the droplet image, which may be relevant to the droplet microstructure. More systematic measurements with the complement of other techniques, such as cryo-EM, would be useful to more clearly characterize the nanoscale microstructure of the droplets.

In summary, by performing molecular simulations, we studied the LLPS of H1 with a focus on the regulation by ssDNA that has the capability to fold into the G4 structure. The phase separation process, including the dynamics of fusion events, was thoroughly characterized in our study (Figure 8). We showed that the fusion of droplets is a rather stochastic process and can be kinetically controlled. The formation of the ssDNA-bridge between two fusing droplets represents the kinetic bottleneck step for the productive fusion event. Furthermore, our study revealed that the microstructure of the condensate is intricately linked to its size as a result of the maximum number of electrostatic contacts. Microphase separation progressively occurs with the increase in droplet sizes. In addition, the stoichiometry of the condensate is also size-dependent, and a larger droplet prefers a stoichiometry with higher ssDNA content. Finally, our study suggests that the increase in multivalency and intermolecule interaction strength between the H1 and ssDNA is a plausible mechanism responsible for the promotion of LLPS by the folding of ssDNA into a G4 structure. These findings offer novel insights into the kinetic processes of LLPS involving proteins and ssDNA, thereby enriching our understanding of biomolecular condensation.

MATERIALS AND METHODS

Models

In this study, residue-resolved coarse-grained models were employed to characterize the protein condensation mediated by ssDNA. For the protein, each residue was represented by one spherical particle centered at the Cα position. The atomic interaction-based coarse-grained model with flexible local interactions (AICG2$^+$)[58,74] was used to describe the dynamics of folded domain of H1, while the hydrophobicity scale model[75] was employed to characterize the interactions involving the intrinsic disordered NTD and CTD. In

https://doi.org/10.1021/jacsau.4c00690
JACS Au 2024, 4, 3690−3704

addition, the three-site-per-nucleotide model (3SPN.2)[76] was adopted for the ssDNA, in which each nucleotide was represented by three particles centered at the phosphate group, the sugar group, and the base group, respectively. To describe the role of G4 structure in LLPS, an additional structure-based potential was added to restrain the ssDNA in the folded G4 conformation following previous work.[77] The reference structure of G4 was taken from a PDB file with the entry 1XAV. The Debye−Hükel-type electrostatic potential was used to characterize the salt-concentration-dependent interactions of charged particles. The combination of AICG2$^+$ and 3SPN models have been successfully used in previous molecular simulations of the structure assembly, functional dynamics, and LLPS of the protein−DNA systems.[32,33,78]

Simulation Details

The simulations were performed with the GENESIS package (version 1.7.1).[79−81] The PDB structures with the entries 7K5Y and 1XAV were used as the references, in building the structured potentials of the H1 and G4 folds, respectively.[82,83] The mixing molar ratio of ssDNA and protein in all the simulations was 5.0 except otherwise stated since the system was found to be most prone to undergo phase separation under this condition in experiments.[47] The simulations were conducted in the *NVT* ensemble except for the ones with spherical boundary restraint. All of the simulations were conducted using the Langevin dynamics with an inverse friction constant of 0.1 ps. The simulation temperature was 300 K and the salt concentration was set to 150 mM. The time step of the MD simulations was 0.01 ps and the total simulation times of condensate dynamics and fusion dynamics were 1×10^8 MD steps and 5×10^7 MD steps, respectively.

To generate droplets of varying sizes, we utilized simulations employing a spherical potential to confine molecules within distinct spatial regions (droplet simulations), mimicking the formation of droplet-like structures. A specific number of H1 chains (N_{H1} = 60, 120, 240, 480, and 960) and the corresponding number of ssDNA chains (N_{DNA} = 300, 600, 1200, 2400, and 4800) were randomly placed in a spherical box. Initially, an equilibrium simulation of 1×10^7 MD steps was performed. Subsequently, a productive simulation of 2×10^7 MD steps was conducted, involving the enlargement of the spherical box radius. Such droplet simulations allowed for the examination of the droplet formation and behavior under varied conditions.

In slab simulations, the system contained 60 chains of H1 and 300 chains of ssDNA, which are sufficient to demonstrate the different phase behaviors of H1 under the regulation of G4 folding. Each system was placed in a periodic box with a long *z*-axis (200 Å × 200 Å × 3600 Å). The initial conformation was a condensed structure obtained from a "shrinking" simulation that squashed the box to 200 Å × 200 Å × 200 Å in 1×10^6 MD steps at 300 K. Both slab simulations for G4-F and G4-U systems started from this conformation. Each slab simulations lasted for 1×10^8 MD steps and the snapshots sampled during the last 5×10^7 MD steps in each trajectory were used in the analysis. In order to evaluate the local density of the slab simulation system, the simulation box was divided into 100 bins along the *z*-axis. Then, the local density was estimated based on the molecule number within each bin. From the density file, the molecules were assigned to be in the dilute phase if the local density is less than a threshold value of 3.4 mM. Similarly, when the local density is higher than the threshold value, the molecules were assigned to be in the condensed phase.

During the clustering of H1 chains in the simulations of condensate formation, we estimated the contacts formed by the proteins and ssDNA molecules for each snapshot. Two H1 monomers were grouped into the same cluster when they interacted with the same ssDNA. A contact was considered to be formed when two beads were within a distance of 5 Å.

In the droplet fusion simulation, the neck structure was defined as the substructure formed by the two droplets from the moment of their initial contact to the point at which stable interactions were established. It was observed that productive fusion occurred when the distance between the two droplets, specifically, the center of mass of the H1 chains in the droplets, was less than 240 Å. As a result, we determined that fusion was considered successful when the two droplets remained within a distance of 240 Å and did not dissociate for a specified duration of MD steps, which was set to 5×10^5 MD steps in this study.

To examine the impact of the ssDNA-bridged substructure formed in the neck-like structure during fusion, we introduced a parameter H. This parameter was defined to characterize the interaction pattern of the ssDNA with the two droplets, utilizing a Hill function. Specifically, H was calculated as the average of H_1 and H_2, where H_i (i = 1,2) was given by $H_i = 1/(1 + e^{-(Q_i - Q_c)/\sigma})$. Here, Q_i represents the contact number between ssDNA and droplet i, which quantifies the extent of contact formation between the ssDNA molecules and the core domains within the neck region. Q_c serves as a cutoff threshold for Q, dictating the formation of stable interactions. Meanwhile, σ is a parameter that modulates the shape of the Hill function. In this work, Q_c and σ were selected as 5.0 and 1.0, respectively. With these defined settings, the resulting H values can effectively quantify the number of droplets to which an ssDNA molecule binds. $H \approx 0.0$ indicates that the ssDNA molecule did not bind to any droplets, whereas $H \approx 0.5$ suggests that the ssDNA molecule is binding to one droplet. When the H value approaches ∼1.0, the ssDNA molecule is binding to two droplets simultaneously, forming an ssDNA-bridge.

Experimental Materials

Histone H1 (H1) from bovine thymus was purchased from Signal Chem (Richmond, BC, Canada). The single-strand DNA (ssDNA) sequence TGAGGGTGGGTAGGGTGGGTAA was obtained from GenScript, Nanjing, China. 1.0 mg/mL H1 solution containing 150 mM NaCl and 50 mM Tris−HCl (pH 7.5) was desalted using a 10,000 MWCO Amicon Ultra centrifugal filter unit (Merck Millipore Ltd., Darmstadt, Germany) into TE buffer (10 mM Tris−HCl, 1 mM EDTA, pH = 7.4) through five centrifugation/dilution cycles. After purification, the concentration of H1 was determined from the absorbance at 280 nm using a Nano-500 microspectrophotometer (Allsheng, Shanghai, China). The ssDNA was dissolved in TE buffer, and the concentration was measured with the same spectrophotometer.

The microscope coverslips for the observation of droplets were obtained from VWR. Before observation, the coverslips were ultrasonic cleaned with 5% detergent for 30 min, followed by two cycles of sonication in ultrapure water for 30 min. The coverslips were dried in a drying oven afterward.

CD Spectra

CD spectra were recorded by using the Chirascan Plus CD spectrometer (Applied Photophysics, UK). Typically, a TE buffer(pH = 7.4) containing 5 μM nucleic acids (ssDNA) with or without 100 mM NaCl/KCl was placed in a 5 mm path-length quartz cuvette for spectrum recording at room temperature. The reported CD spectra were averaged from three scans with a response time of 1 s and a spectral bandwidth of 1.0 nm to increase the signal-to-noise ratio. The results were expressed as molar ellipticity [θ].

Transmission Electron Microscopy Imaging

Total volume of a 5 μL solution containing 2 μM H1 and 20 μM ssDNA in TE buffer (pH = 7.4) was mixed in a centrifuge tube and dropped onto carbon-coated copper grid immediately after a brief vortex-mix. After incubation for 1 h at room temperature, the copper grid containing the samples was transferred to a 37 °C incubator for drying for 1 h. After cooling, the grid was stained with 1% uranyl acetate. EM images were observed on an FEI Talos F200 S G2 TEM (FEI, USA) at an accelerating voltage of 200 kV. The experiment was repeated three times.

Single-Molecule FRET Imaging

PEG/biotin-PEG passivated coverslips were used to construct home-built flow cells, as described previously.[84] The coverslips were functionalized by incubating the imaging chamber with 0.1 mg/mL streptavidin. Cy5-labeled ssDNA containing PU22 sequence (5′-Cy5-TGAGGGTGGGTAGGGTGGG TAAAGAGGTAAAAGGA-

https://doi.org/10.1021/jacsau.4c00690
JACS Au 2024, 4, 3690−3704

TAATGGCCACGGTGCG-3′) was annealed to a holding ssDNA strand labeled with Cy3 and biotin (5′ Biotin-CGCACCGTGGC-CATTAT CCTTT/iCy3-dT/ACCTCT-3′) and then attached to the coverslip surface through streptavidin−biotin interactions. The samples were imaged using an IX-71 based objective-type total internal reflection fluorescence microscope with an oil immersion UAPON 100XOTIRF objective lens (N.A. = 1.49, Olympus). A 532 nm laser was used for the excitation of Cy3. The emission fluorescence was split into two channels by a dichroic mirror (FF649-Di01, Semrock), and two band-pass filters (FF01-585/40 and FF01-675/67, Semrock) were used for the green and red emission channels, respectively. The signal was collected by an EMCCD camera (IXon 897, Andor Technology) with a temporal resolution of 50 ms. All experiments were performed at room temperature in an imaging buffer of 10 mM Tris−HCl (pH 7.5) with indicated salt concentrations and the addition of an oxygen scavenging system containing 25 mM protocatechuate acid (PCA; Sigma), 25 nM protocatechuate-3,4-dioxygenase (PCD; Sigma), and the triplet-state quenching reagent (2 mM Trolox, Sigma). Each data set containing more than 1000 traces was collected from at least three independent experiments.

Bright Field Microscopy Imaging of Droplets

A stock solution of H1 (∼25 μM) and ssDNA (∼200 μM) was used to prepare the sample. Total volume of a 15 μL solution containing 2 μM H1 and 11 μM ssDNA in TE buffer (pH = 7.4) with different salt concentrations was mixed in a centrifuge tube and transferred to the observation well immediately after a brief vortex-mix. The samples were observed after incubation for 30 min. Images were obtained using an inverted microscope equipped with a Basler camera (NexcopeNIB610-FL) and official Basler software. In the experiments characterizing the effect of later addition of extra ssDNA, the initial solutions contain 11 μM (Exp-1 and Exp-2) or 12 μM (Exp-3) ssDNA and 2 μM H1 (Figure S4). All experiments were repeated three times. The images were analyzed by using ImageJ.

For confocal imaging, the Cy5-labeled ssDNA stock solution was prepared with a labeling ratio of 1000:1. Similarly, we also prepared the Cy3-labeled ssDNA stock solution with the same labeling ratio. After the incubation of the solution containing 2 μM H1 and 11 μM Cy5-labeled ssDNA in TE buffer for 5 min, additional solution containing 1 μM Cy3-labeled ssDNA was added. The sample was imaged with a spin-disk confocal microscope (Nikon X-Light V3, 100× oil objective). The laser power was set at 40% to reduce photobleaching.

■ ASSOCIATED CONTENT

Data Availability Statement

The MD simulation files and data analysis scripts are available at https://github.com/yunqiang Bian/llps-G4-H1.

Supporting Information

The Supporting Information is available free of charge at https://pubs.acs.org/doi/10.1021/jacsau.4c00690.

Additional results of MD simulation and experimental measurements (PDF)

■ AUTHOR INFORMATION

Corresponding Authors

Wenfei Li − *Wenzhou Key Laboratory of Biophysics, Wenzhou Institute, University of Chinese Academy of Sciences, Wenzhou 325000 Zhejiang, China; Department of Physics, National Laboratory of Solid State Microstructure, Nanjing University, Nanjing 210093, China;* orcid.org/0000-0003-2679-4075; Email: wfli@nju.edu.cn

Wei Wang − *Department of Physics, National Laboratory of Solid State Microstructure, Nanjing University, Nanjing 210093, China;* orcid.org/0000-0001-5441-0302; Email: wangwei@nju.edu.cn

Authors

Yunqiang Bian − *Wenzhou Key Laboratory of Biophysics, Wenzhou Institute, University of Chinese Academy of Sciences, Wenzhou 325000 Zhejiang, China;* orcid.org/0000-0002-7316-8301

Fangyi Lv − *Wenzhou Key Laboratory of Biophysics, Wenzhou Institute, University of Chinese Academy of Sciences, Wenzhou 325000 Zhejiang, China; Department of Physics, Wenzhou University, Wenzhou 325035, China*

Hai Pan − *Wenzhou Key Laboratory of Biophysics, Wenzhou Institute, University of Chinese Academy of Sciences, Wenzhou 325000 Zhejiang, China;* orcid.org/0000-0001-6660-9052

Weitong Ren − *Wenzhou Key Laboratory of Biophysics, Wenzhou Institute, University of Chinese Academy of Sciences, Wenzhou 325000 Zhejiang, China*

Weiwei Zhang − *Wenzhou Key Laboratory of Biophysics, Wenzhou Institute, University of Chinese Academy of Sciences, Wenzhou 325000 Zhejiang, China*

Yanwei Wang − *Department of Physics, Wenzhou University, Wenzhou 325035, China*

Yi Cao − *Department of Physics, National Laboratory of Solid State Microstructure, Nanjing University, Nanjing 210093, China; Wenzhou Key Laboratory of Biophysics, Wenzhou Institute, University of Chinese Academy of Sciences, Wenzhou 325000 Zhejiang, China;* orcid.org/0000-0003-1493-7868

Complete contact information is available at: https://pubs.acs.org/10.1021/jacsau.4c00690

Author Contributions

‖Y.B., F.L., and H.P. contributed equally to this paper. Conceptualization: Y.B., W.L., and W.W. Investigation: Y.B., F.L., and H.P. Data curation: Y.B. and F.L. Analysis and visualization: Y.B., F.L., H.P., W.R., W.Z., Y.W., and Y.C. Writing: Y.B., W.L., and W.W.

Notes

The authors declare no competing financial interest.

■ ACKNOWLEDGMENTS

The authors thank Zhi Qi and Cheng Li for insightful comments. This work was supported by National Natural Science Foundation of China (grant nos. 11974173 and 11934008), the grant of Wenzhou Institute, University of Chinese Academy of Sciences (WIUCASQD2021010, WIUCASQD2022036, WIUCASQD2022003, and WIUCASQD2023015), and Natural Science Foundation of Shandong Province (grant no. ZR202102210546). The authors also thank the support of High Performance Computing Center of Nanjing University.

■ REFERENCES

(1) Banani, S. F.; Lee, H. O.; Hyman, A. A.; Rosen, M. K. Biomolecular condensates: organizers of cellular biochemistry. *Nat. Rev. Mol. Cell Biol.* **2017**, *18*, 285−298.

(2) Shin, Y.; Brangwynne, C. P. Liquid phase condensation in cell physiology and disease. *Science* **2017**, *357*, No. eaaf4382.

(3) Erdel, F.; Rippe, K. Formation of Chromatin Subcompartments by Phase Separation. *Biophys. J.* **2018**, *114*, 2262−2270.

(4) Zhang, H.; Ji, X.; Li, P.; Liu, C.; Lou, J.; Wang, Z.; Wen, W.; Xiao, Y.; Zhang, M.; Zhu, X. Liquid-liquid phase separation in biology: mechanisms, physiological functions and human diseases. *Sci. China: Life Sci.* **2020**, *63*, 953−985.
(5) Folkmann, A. W.; Putnam, A.; Lee, C. F.; Seydoux, G. Regulation of biomolecular condensates by interfacial protein clusters. *Science* **2021**, *373*, 1218−1224.
(6) Brangwynne, C. P.; Eckmann, C. R.; Courson, D. S.; Rybarska, A.; Hoege, C.; Gharakhani, J.; Jülicher, F.; Hyman, A. A. Germline P Granules Are Liquid Droplets That Localize by Controlled Dissolution/Condensation. *Science* **2009**, *324*, 1729−1732.
(7) Feric, M.; Vaidya, N.; Harmon, T. S.; Mitrea, D. M.; Zhu, L.; Richardson, T. M.; Kriwacki, R. W.; Pappu, R. V.; Brangwynne, C. P. Coexisting Liquid Phases Underlie Nucleolar Subcompartments. *Cell* **2016**, *165*, 1686−1697.
(8) Larson, A. G.; Elnatan, D.; Keenen, M. M.; Trnka, M. J.; Johnston, J. B.; Burlingame, A. L.; Agard, D. A.; Redding, S.; Narlikar, G. J. Liquid droplet formation by HP1α suggests a role for phase separation in heterochromatin. *Nature* **2017**, *547*, 236−240.
(9) Latham, A. P.; Zhang, B. On the stability and layered organization of protein-DNA condensates. *Biophys. J.* **2022**, *121*, 1727−1737.
(10) Riback, J. A.; Zhu, L.; Ferrolino, M. C.; Tolbert, M.; Mitrea, D. M.; Sanders, D. W.; Wei, M.-T.; Kriwacki, R. W.; Brangwynne, C. P. Composition-dependent thermodynamics of intracellular phase separation. *Nature* **2020**, *581*, 209−214.
(11) Boeynaems, S.; Alberti, S.; Fawzi, N. L.; Mittag, T.; Polymenidou, M.; Rousseau, F.; Schymkowitz, J.; Shorter, J.; Wolozin, B.; Van Den Bosch, L.; Tompa, P.; Fuxreiter, M. Protein Phase Separation: A New Phase in Cell Biology. *Trends Cell Biol.* **2018**, *28*, 420−435.
(12) Patel, A.; Lee, H. O.; Jawerth, L.; Maharana, S.; Jahnel, M.; Hein, M. Y.; Stoynov, S.; Mahamid, J.; Saha, S.; Franzmann, T. M.; Pozniakovski, A.; Poser, I.; Maghelli, N.; Royer, L. A.; Weigert, M.; Myers, E. W.; Grill, S.; Drechsel, D.; Hyman, A. A.; Alberti, S. A liquid-to-solid phase transition of the ALS protein FUS accelerated by disease mutation. *Cell* **2015**, *162*, 1066−1077.
(13) Molliex, A.; Temirov, J.; Lee, J.; Coughlin, M.; Kanagaraj, A.; Kim, H.; Mittag, T.; Taylor, J. Phase Separation by Low Complexity Domains Promotes Stress Granule Assembly and Drives Pathological Fibrillization. *Cell* **2015**, *163*, 123−133.
(14) Burke, K.; Janke, A.; Rhine, C.; Fawzi, N. Residue-by-Residue View of In Vitro FUS Granules that Bind the C-Terminal Domain of RNA Polymerase II. *Mol. Cell* **2015**, *60*, 231−241.
(15) Hyman, A. A.; Weber, C. A.; Jülicher, F. Liquid-Liquid Phase Separation in Biology. *Annu. Rev. Cell Dev. Biol.* **2014**, *30*, 39−58.
(16) Brangwynne, C. P.; Tompa, P.; Pappu, R. Polymer physics of intracellular phase transitions. *Nat. Phys.* **2015**, *11*, 899−904.
(17) Choi, J.-M.; Holehouse, A. S.; Pappu, R. V. Physical Principles Underlying the Complex Biology of Intracellular Phase Transitions. *Annu. Rev. Biophys.* **2020**, *49*, 107−133.
(18) Dignon, G. L.; Best, R. B.; Mittal, J. Biomolecular Phase Separation: From Molecular Driving Forces to Macroscopic Properties. *Annu. Rev. Phys. Chem.* **2020**, *71*, 53−75.
(19) Dignon, G. L.; Zheng, W.; Kim, Y. C.; Mittal, J. Temperature-Controlled Liquid−Liquid Phase Separation of Disordered Proteins. *ACS Cent. Sci.* **2019**, *5*, 821−830.
(20) Harami, G. M.; Kovács, Z. J.; Pancsa, R.; Pálinkás, J.; Baráth, V.; Tárnok, K.; Málnási-Csizmadia, A.; Kovács, M. Phase separation by ssDNA binding protein controlled via protein-protein and protein-DNA interactions. *Proc. Natl. Acad. Sci. U.S.A.* **2020**, *117*, 26206−26217.
(21) Chu, W.-T.; Wang, J. Thermodynamic and sequential characteristics of phase separation and droplet formation for an intrinsically disordered region/protein ensemble. *PLoS Comput. Biol.* **2021**, *17*, No. e1008672.
(22) Banks, A.; Qin, S.; Weiss, K. L.; Stanley, C. B.; Zhou, H. X. Intrinsically Disordered Protein Exhibits Both Compaction and Expansion under Macromolecular Crowding. *Biophys. J.* **2018**, *114*, 1067−1079.
(23) Harmon, T. S.; Holehouse, A. S.; Rosen, M. K.; Pappu, R. V. Intrinsically disordered linkers determine the interplay between phase separation and gelation in multivalent proteins. *eLife* **2017**, *6*, No. e30294.
(24) Cinar, S.; Cinar, H.; Chan, H. S.; Winter, R. Pressure-sensitive and osmolyte-modulated liquid−liquid phase separation of eye-lens γ-crystallins. *J. Am. Chem. Soc.* **2019**, *141*, 7347−7354.
(25) Le Ferrand, H.; Duchamp, M.; Gabryelczyk, B.; Cai, H.; Miserez, A. Time-resolved observations of liquid-liquid phase separation at the nanoscale using in situ liquid transmission electron microscopy. *J. Am. Chem. Soc.* **2019**, *141*, 7202−7210.
(26) von Bülow, S.; Siggel, M.; Linke, M.; Hummer, G. Dynamic cluster formation determines viscosity and diffusion in dense protein solutions. *Proc. Natl. Acad. Sci. U.S.A.* **2019**, *116*, 9843−9852.
(27) Ghosh, A.; Kota, D.; Zhou, H.-X. Shear relaxation governs fusion dynamics of biomolecular condensates. *Nat. Commun.* **2021**, *12*, 5995.
(28) Delarue, M.; Brittingham, G. P.; Pfeffer, S.; Surovtsev, I.; Pinglay, S.; Kennedy, K.; Schaffer, M.; Gutierrez, J.; Sang, D.; Poterewicz, G.; Chung, J. K.; Plitzko, J. M.; Groves, J. T.; Jacobs-Wagner, C.; Engel, B. D.; Holt, L. J. mTORC1 controls phase separation and the biophysical properties of the cytoplasm by tuning crowding. *Cell* **2018**, *174*, 338−349.e20.
(29) Gu, R. X.; Baoukina, S.; Tieleman, D. P. Phase Separation in Atomistic Simulations of Model Membranes. *J. Am. Chem. Soc.* **2020**, *142*, 2844−2856.
(30) Conicella, A. E.; Dignon, G. L.; Zerze, G. H.; Schmidt, H. B.; D'Ordine, A. M.; Kim, Y. C.; Rohatgi, R.; Ayala, Y. M.; Mittal, J.; Fawzi, N. L. TDP-43 α-helical structure tunes liquid−liquid phase separation and function. *Proc. Natl. Acad. Sci. U.S.A.* **2020**, *117*, 5883−5894.
(31) Jin, J.; Yu, A.; Voth, G. A. Temperature and Phase Transferable Bottom-up Coarse-Grained Models. *J. Chem. Theory Comput.* **2020**, *16*, 6823−6842.
(32) Tan, C.; Niitsu, A.; Sugita, Y. Highly Charged Proteins and Their Repulsive Interactions Antagonize Biomolecular Condensation. *JACS Au* **2023**, *3*, 834−848.
(33) Mizutani, A.; Tan, C.; Sugita, Y.; Takada, S. Micelle-like clusters in phase-separated Nanog condensates: A molecular simulation study. *PLoS Comput. Biol.* **2023**, *19*, No. e1011321.
(34) Latham, A. P.; Zhu, L.; Sharon, D. A.; Ye, S.; Willard, A. P.; Zhang, X.; Zhang, B. Frustrated Microphase Separation Produces Interfacial Environment within Biological Condensates. *eLife* **2023**, *12*, RP90750.
(35) Zhang, H.; Elbaum-Garfinkle, S.; Langdon, E. M.; Taylor, N.; Occhipinti, P.; Bridges, A.; Brangwynne, C.; Gladfelter, A. RNA Controls PolyQ Protein Phase Transitions. *Mol. Cell* **2015**, *60*, 220−230.
(36) King, J. T.; Shakya, A. Phase separation of DNA: From past to present. *Biophys. J.* **2021**, *120*, 1139−1149.
(37) Lin, Y.; Protter, D.; Rosen, M.; Parker, R. Formation and Maturation of Phase-Separated Liquid Droplets by RNA-Binding Proteins. *Mol. Cell* **2015**, *60*, 208−219.
(38) McSwiggen, D. T.; Hansen, A. S.; Teves, S. S.; Marie-Nelly, H.; Hao, Y.; Heckert, A. B.; Umemoto, K. K.; Dugast-Darzacq, C.; Tjian, R.; Darzacq, X. Evidence for DNA-mediated nuclear compartmentalization distinct from phase separation. *eLife* **2019**, *8*, No. e47098.
(39) Patel, A.; Malinovska, L.; Saha, S.; Wang, J.; Alberti, S.; Krishnan, Y.; Hyman, A. A. ATP as a biological hydrotrope. *Science* **2017**, *356*, 753−756.
(40) Han, T.; Kato, M.; Xie, S.; Wu, L.; Mirzaei, H.; Pei, J.; Chen, M.; Xie, Y.; Allen, J.; Xiao, G.; McKnight, S. Cell-free Formation of RNA Granules: Bound RNAs Identify Features and Components of Cellular Assemblies. *Cell* **2012**, *149*, 768−779.
(41) Maharana, S.; Wang, J.; Papadopoulos, D. K.; Richter, D.; Pozniakovsky, A.; Poser, I.; Bickle, M.; Rizk, S.; Guillén-Boixet, J.; Franzmann, T. M.; Jahnel, M.; Marrone, L.; Chang, Y.-T.; Sterneckert,

https://doi.org/10.1021/jacsau.4c00690
JACS Au 2024, 4, 3690−3704

J.; Tomancak, P.; Hyman, A. A.; Alberti, S. RNA buffers the phase separation behavior of prion-like RNA binding proteins. *Science* **2018**, *360*, 918−921.
(42) Mimura, M.; Tomita, S.; Sugai, H.; Shinkai, Y.; Ishihara, S.; Kurita, R. Uncharged components of single-stranded DNA modulate liquid−liquid phase separation with cationic linker histone H1. *Front. Cell Dev. Biol.* **2021**, *9*, 710729.
(43) Spegg, V.; Panagopoulos, A.; Stout, M.; Krishnan, A.; Reginato, G.; Imhof, R.; Roschitzki, B.; Cejka, P.; Altmeyer, M. Phase separation properties of RPA combine high-affinity ssDNA binding with dynamic condensate functions at telomeres. *Nat. Struct. Mol. Biol.* **2023**, *30*, 451−462.
(44) Leicher, R.; Osunsade, A.; Chua, G. N. L.; Faulkner, S. C.; Latham, A. P.; Watters, J. W.; Nguyen, T.; Beckwitt, E. C.; Christodoulou-Rubalcava, S.; Young, P. G.; Zhang, B.; David, Y.; Liu, S. Single-stranded nucleic acid binding and coacervation by linker histone H1. *Nat. Struct. Mol. Biol.* **2022**, *29*, 463−471.
(45) Fyodorov, D. V.; Zhou, B.-R.; Skoultchi, A. I.; Bai, Y. Emerging roles of linker histones in regulating chromatin structure and function. *Nat. Rev. Mol. Cell Biol.* **2018**, *19*, 192−206.
(46) Turner, A. L.; Watson, M.; Wilkins, O. G.; Cato, L.; Travers, A.; Thomas, J. O.; Stott, K. Highly disordered histone H1-DNA model complexes and their condensates. *Proc. Natl. Acad. Sci. U.S.A.* **2018**, *115*, 11964−11969.
(47) Mimura, M.; Tomita, S.; Shinkai, Y.; Hosokai, T.; Kumeta, H.; Saio, T.; Shiraki, K.; Kurita, R. Quadruplex Folding Promotes the Condensation of Linker Histones and DNAs via Liquid−Liquid Phase Separation. *J. Am. Chem. Soc.* **2021**, *143*, 9849−9857.
(48) Hackett, J. A.; Feldser, D. M.; Greider, C. W. Telomere Dysfunction Increases Mutation Rate and Genomic Instability. *Cell* **2001**, *106*, 275−286.
(49) Balasubramanian, S.; Hurley, L. H.; Neidle, S. Targeting G-quadruplexes in gene promoters: a novel anticancer strategy? *Nat. Rev. Drug Discovery* **2011**, *10*, 261−275.
(50) Hoffmann, R. F.; Moshkin, Y. M.; Mouton, S.; Grzeschik, N. A.; Kalicharan, R. D.; Kuipers, J.; Wolters, A. H. G.; Nishida, K.; Romashchenko, A. V.; Postberg, J.; Lipps, H.; Berezikov, E.; Sibon, O. C. M.; Giepmans, B. N. G.; Lansdorp, P. M. Guanine quadruplex structures localize to heterochromatin. *Nucleic Acids Res.* **2016**, *44*, 152−163.
(51) Liu, X.; Xiong, Y.; Zhang, C.; Lai, R.; Liu, H.; Peng, R.; Fu, T.; Liu, Q.; Fang, X.; Mann, S.; Tan, W. G-Quadruplex-Induced Liquid−Liquid Phase Separation in Biomimetic Protocells. *J. Am. Chem. Soc.* **2021**, *143*, 11036−11043.
(52) Ambrus, A.; Chen, D.; Dai, J.; Jones, R. A.; Yang, D. Solution Structure of the Biologically Relevant G-Quadruplex Element in the Human c-MYC Promoter. Implications for G-Quadruplex Stabilization. *Biochemistry* **2005**, *44*, 2048−2058.
(53) Siggia, E. D. Late stages of spinodal decomposition in binary mixtures. *Phys. Rev. A* **1979**, *20*, 595−605.
(54) Lifshitz, I.; Slyozov, V. The kinetics of precipitation from supersaturated solid solutions. *J. Phys. Chem. Solids* **1961**, *19*, 35−50.
(55) Berry, J.; Weber, S. C.; Vaidya, N.; Haataja, M.; Brangwynne, C. P. RNA transcription modulates phase transition-driven nuclear body assembly. *Proc. Natl. Acad. Sci. U.S.A.* **2015**, *112*, E5237−E5245.
(56) Alberti, S.; Gladfelter, A.; Mittag, T. Considerations and Challenges in Studying Liquid-Liquid Phase Separation and Biomolecular Condensates. *Cell* **2019**, *176*, 419−434.
(57) Ferreiro, D. U.; Komives, E. A.; Wolynes, P. G. Frustration in biomolecules. *Q. Rev. Biophys.* **2014**, *47*, 285−363.
(58) Li, W.; Wolynes, P. G.; Takada, S. Frustration, specific sequence dependence, and nonlinearity in large-amplitude fluctuations of allosteric proteins. *Proc. Natl. Acad. Sci. U.S.A.* **2011**, *108*, 3504−3509.
(59) Kim, B. G.; Evans, H. M.; Dubins, D. N.; Chalikian, T. V. Effects of salt on the stability of a G-quadruplex from the human c-MYC promoter. *Biochemistry* **2015**, *54*, 3420−3430.
(60) Ghosh, A.; Zhou, H.-X. Determinants for fusion speed of biomolecular droplets. *Angew. Chem., Int. Ed. Engl.* **2020**, *59*, 20837−20840.
(61) Navarro, M. G.-J.; Kashida, S.; Chouaib, R.; Souquere, S.; Pierron, G.; Weil, D.; Gueroui, Z. RNA is a critical element for the sizing and the composition of phase-separated RNA−protein condensates. *Nat. Commun.* **2019**, *10*, 3230.
(62) Tauber, D.; Tauber, G.; Khong, A.; Van Treeck, B.; Pelletier, J.; Parker, R. Modulation of RNA Condensation by the DEAD-Box Protein eIF4A. *Cell* **2020**, *180*, 411−426.e16.
(63) Putnam, A.; Cassani, M.; Smith, J.; Seydoux, G. A gel phase promotes condensation of liquid P granules in Caenorhabditis elegans embryos. *Nat. Struct. Mol. Biol.* **2019**, *26*, 220−226.
(64) Cirillo, L.; Cieren, A.; Barbieri, S.; Khong, A.; Schwager, F.; Parker, R.; Gotta, M. UBAP2L forms distinct cores that act in nucleating stress granules upstream of G3BP1. *Curr. Biol.* **2020**, *30*, 698−707.e6.
(65) Shen, Y.; Chen, A.; Wang, W.; Shen, Y.; Ruggeri, F. S.; Aime, S.; Wang, Z.; Qamar, S.; Espinosa, J. R.; Garaizar, A.; St George-Hyslop, P.; Collepardo-Guevara, R.; Weitz, D. A.; Vigolo, D.; Knowles, T. P. J. The liquid-to-solid transition of FUS is promoted by the condensate surface. *Proc. Natl. Acad. Sci. U.S.A.* **2023**, *120*, No. e2301366120.
(66) Kistler, K. E.; Trcek, T.; Hurd, T. R.; Chen, R.; Liang, F.-X.; Sall, J.; Kato, M.; Lehmann, R. Phase transitioned nuclear Oskar promotes cell division of Drosophila primordial germ cells. *eLife* **2018**, *7*, No. e37949.
(67) Alshareedah, I.; Moosa, M. M.; Raju, M.; Potoyan, D. A.; Banerjee, P. R. Phase transition of RNA-protein complexes into ordered hollow condensates. *Proc. Natl. Acad. Sci. U.S.A.* **2020**, *117*, 15650−15658.
(68) Das, R.; Sakaue, T.; Shivashankar, G. V.; Prost, J.; Hiraiwa, T. How enzymatic activity is involved in chromatin organization. *eLife* **2022**, *11*, No. e79901.
(69) Schuster, B. S.; Regy, R. M.; Dolan, E. M.; Kanchi Ranganath, A.; Jovic, N.; Khare, S. D.; Shi, Z.; Mittal, J. Biomolecular condensates: Sequence determinants of phase separation, microstructural organization, enzymatic activity, and material properties. *J. Phys. Chem. B* **2021**, *125*, 3441−3451.
(70) Ranganathan, S.; Shakhnovich, E. I. Dynamic metastable long-living droplets formed by sticker-spacer proteins. *eLife* **2020**, *9*, No. e56159.
(71) Forman-Kay, J. D.; Ditlev, J. A.; Nosella, M. L.; Lee, H. O. What are the distinguishing features and size requirements of biomolecular condensates and their implications for RNA-containing condensates? *RNA* **2022**, *28*, 36−47.
(72) Fox, A. H.; Lam, Y. W.; Leung, A. K.; Lyon, C. E.; Andersen, J.; Mann, M.; Lamond, A. I. Paraspeckles: a novel nuclear domain. *Curr. Biol.* **2002**, *12*, 13−25.
(73) Cho, W.-K.; Spille, J.-H.; Hecht, M.; Lee, C.; Li, C.; Grube, V.; Cisse, I. I. Mediator and RNA polymerase II clusters associate in transcription-dependent condensates. *Science* **2018**, *361*, 412−415.
(74) Li, W.; Wang, W.; Takada, S. Energy landscape views for interplays among folding, binding, and allostery of calmodulin domains. *Proc. Natl. Acad. Sci. U.S.A.* **2014**, *111*, 10550−10555.
(75) Dignon, G. L.; Zheng, W.; Kim, Y. C.; Best, R. B.; Mittal, J. Sequence determinants of protein phase behavior from a coarse-grained model. *PLoS Comput. Biol.* **2018**, *14*, No. e1005941.
(76) Hinckley, D. M.; Freeman, G. S.; Whitmer, J. K.; de Pablo, J. J. An experimentally-informed coarse-grained 3-site-per-nucleotide model of DNA: Structure, thermodynamics, and dynamics of hybridization. *J. Chem. Phys.* **2013**, *139*, 144903.
(77) Clementi, C.; Nymeyer, H.; Onuchic, J. N. Topological and energetic factors: what determines the structural details of the transition state ensemble and "en-route" intermediates for protein folding? An investigation for small globular proteins. *J. Mol. Biol.* **2000**, *298*, 937−953.

https://doi.org/10.1021/jacsau.4c00690
JACS Au 2024, 4, 3690−3704

(78) Lequieu, J.; Schwartz, D. C.; De Pablo, J. J. In silico evidence for sequence-dependent nucleosome sliding. *Proc. Natl. Acad. Sci. U.S.A.* **2017**, *114*, E9197−E9205.
(79) Jung, J.; Mori, T.; Kobayashi, C.; Matsunaga, Y.; Yoda, T.; Feig, M.; Sugita, Y. GENESIS: a hybrid-parallel and multi-scale molecular dynamics simulator with enhanced sampling algorithms for biomolecular and cellular simulations. *Wiley Interdiscip. Rev.: Comput. Mol. Sci.* **2015**, *5*, 310−323.
(80) Kobayashi, C.; Jung, J.; Matsunaga, Y.; Mori, T.; Ando, T.; Tamura, K.; Kamiya, M.; Sugita, Y. GENESIS 1.1: A hybrid-parallel molecular dynamics simulator with enhanced sampling algorithms on multiple computational platforms. *J. Comput. Chem.* **2017**, *38*, 2193−2206.
(81) Tan, C.; Jung, J.; Kobayashi, C.; Torre, D. U. L.; Takada, S.; Sugita, Y. Implementation of residue-level coarse-grained models in GENESIS for large-scale molecular dynamics simulations. *PLoS Comput. Biol.* **2022**, *18*, No. e1009578.
(82) Zhou, B.-R.; Feng, H.; Kale, S.; Fox, T.; Khant, H.; de Val, N.; Ghirlando, R.; Panchenko, A. R.; Bai, Y. Distinct Structures and Dynamics of Chromatosomes with Different Human Linker Histone Isoforms. *Mol. Cell* **2021**, *81*, 166−182.e6.
(83) Mathad, R. I.; Hatzakis, E.; Dai, J.; Yang, D. c-MYC promoter G-quadruplex formed at the 5′-end of NHE III 1 element: insights into biological relevance and parallel-stranded G-quadruplex stability. *Nucleic Acids Res.* **2011**, *39*, 9023−9033.
(84) Pan, H.; Xia, Y.; Qin, M.; Cao, Y.; Wang, W. A simple procedure to improve the surface passivation for single molecule fluorescence studies. *Phys. Biol.* **2015**, *12*, 045006.

https://doi.org/10.1021/jacsau.4c00690
JACS Au 2024, 4, 3690−3704